



Contents lists available at ScienceDirect

Journal of the Mechanics and Physics of Solids

journal homepage: www.elsevier.com/locate/jmps

Geometry and mechanics of inextensible curvilinear balloons

Emmanuel Siéfert*, José Bico, Etienne Reyssat, Benoît Roman

PMMH, CNRS, ESPCI Paris, Université PSL, Sorbonne Université, Université de Paris, F-75005, Paris, France



ARTICLE INFO

Article history:

Received 26 February 2020
 Revised 23 June 2020
 Accepted 26 June 2020
 Available online 27 June 2020

Keywords:

Tension field theory
 Wrinkles
 Inflated structures
 Lagrangian optimization
 Inverse problem

ABSTRACT

Mylar balloons are popular in funfairs or birthday parties. Their conception is very simple: two pieces of flat thin sheets are cut and sealed together along their edges to form a flat envelope. Inflation tends to deform this envelope in order to maximize its inner volume. However, although thin sheets are easy to bend and hardly resist compressive loads, they barely stretch, which imposes non-trivial geometrical constraints. Such thin sheets are generally described under the framework of “tension field theory” where their stiffness is considered as infinite under stretching and vanishes under compression or bending. In this study, we focus on the shape after inflation of flat, curved templates of constant width. Counter-intuitively, the curvatures of the paths tend to increase upon inflation, which leads to out of plane buckling of non-confined closed structures. After determining the optimal cross section of axisymmetric annuli, we predict the change in local curvature induced in open paths. We finally describe the location of wrinkled and smooth areas observed in inflated structures that correspond to compression and tension, respectively.

© 2020 Elsevier Ltd. All rights reserved.

1. Introduction

Inflated structures present several advantages such as high stiffness-to-weight ratio, efficient storage, quick deployment and cost efficiency. They are widely used in a broad range of applications, such as lightweight tents, in which rigid poles are replaced by air beams, scientific ballooning (Pagitz and Pellegrino, 2007a; 2007b), stent deployment in angioplasty (Serruys et al., 1994), ultralight deployable structures for space exploration (Pellegrino, 2014) and soft robotics (Hawkes et al., 2017; Rus and Tolley, 2015). Thin-walled inflated structures may be separated into two mechanical regimes depending on the magnitude of membrane strains induced by pressure. In a first regime, when $p \sim Et/L$ (where p is the inflating pressure, E the Young modulus of the envelope material, t the typical thickness of the envelope and L the smallest typical size of a structure unit), the envelope is strongly stretched and typical strains are finite. This configuration is relevant to elastomers that can accommodate finite stretching without failure. This hyperelastic regime has been recently investigated in numerous studies concerning soft robotics (Shepherd et al., 2011; Siéfert et al., 2019a), the propagation of bulges (Chater and Hutchinson, 1984; Kyriakides and Yu-Chung, 1991), or the shape and stability of toroidal membranes (Roychowdhury and DasGupta, 2015; 2018; Tamadapu and DasGupta, 2013). We note that such elastomer structures remain however intrinsically soft and cannot sustain their own weight at large scale, since the typical Young modulus of the material used is of the order of a few MPa. Large inflated structures thus belong to a second regime $p \ll Et/L$, and can be separated in two other subcases depending on the ability of pressure forces to bend the envelope of the structure. In the first regime, stiff

* Corresponding author at: Laboratoire de Physique et Mécanique des Milieux Hétérogènes (PMMH), CNRS UMR 7636, ESPCI Paris, PSL Research University, 10 rue Vauquelin, Paris, France.

E-mail address: emmanuel.siefert@espci.fr (E. Siéfert).

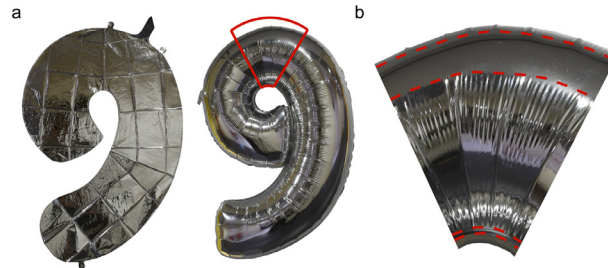


Fig. 1. Curvilinear mylar balloon. **a.** The number “9” before and after inflation: the initially open outline over-curves when inflated and self-contact appears, closing the nine. **b.** Details of the wrinkling pattern on the envelope: hierarchical radial wrinkles appear except on two parts (delimited by red dashed lines): at the inner seam and along a wider band between the mid line and the outer seam, the latter being compressed. (For interpretation of the references to colour in this figure legend, the reader is referred to the web version of this article.)

engineering structures, such as tanks and shells, are designed to sustain pressure without large deflections (Kiefner, 1973). In this case the typical deflection scales as $\delta \sim pL/(Et^3/L^3)$, where pL is the force (per unit width) applied by pressure, and Et^3/L^3 is the typical bending stiffness of a structure with length L (per unit width). This regime therefore holds when $\delta \ll L$, or equivalently $p \ll Et^3/L^3$. In the other limit, $p \gg Et^3/L^3$, the bending stiffness of the structure cannot sustain pressure loads.

The present study focuses on the doubly asymptotic regime $Et^3/L^3 \ll p \ll Et/L$, where the envelope is quasi-inextensible but infinitely bendable. In this regime, the envelope can accommodate compression at almost no cost by forming wrinkles or folds that may be viewed as a “decoration” (King et al., 2012; Steigmann, 1990). Following the seminal study of the shape of parachutes by Taylor (1963), theoretical work has been dedicated to the shape of inflated circular disks (Ligaro and Barsotti, 2008; Paulsen, 1994), polyhedral surfaces (Pak, 2006), and instabilities in scientific balloons (Deng, 2012; Pagitz and Pellegrino, 2007a). Recent progress has been achieved in solving numerically the inverse problem, that is programming the envelope made of a collection of flat panels seamed together, in order to morph onto a target shape upon inflation (Skouras et al., 2014). Here, we experimentally and theoretically investigate the shapes of initially flat annuli and, more generally, of any curvilinear path such as balloon numbers or letters (Fig. 1a). This study generalizes a preliminary work presented in reference (Siéfert et al., 2019b), where the families of cross section in open and closed configurations were assumed to be identical.

Mylar balloons exhibit non-intuitive features that we wish to rationalize. As a striking result, the curvature of the outline of the structures tends to increase upon inflation: the initially open template of a number “9” balloon closes when inflated (Fig. 1). Radial wrinkles present in most of the envelope indicate compressive strains, which may appear counter-intuitive for a structure under pressure. Nonetheless, wrinkles are absent along two up-down symmetric bands that follow the outline of the structure and in the vicinity of the inner seam (red regions highlighted in Fig. 1b).

In this article, we aim at understanding the inflation-induced coiling of the outline, the shape of the cross sections, and the location of radial wrinkles (i.e. the strain distribution along the envelope). The structures are made from two superimposed identical curved, flat templates, seam-welded together along their boundary. We first derive the equations for the equilibrium shape of an inflated axisymmetric flat ring, using two methods : a variational volume maximization, or a direct force balance. The predicted cross-sections are quantitatively compared with the experiments on closed rings. We then extend our model to open circular rings and to arbitrary curved paths, where coiling is allowed, and relate the orientation and extension of wrinkles to the direction and location of compression. We finally solve the inverse problem, *i. e.* we find the flat reference state that will deform onto a target outline upon inflation, and test it on a few examples.

2. Inflating closed rings

The fabrication process consists in sealing two layers of thermosealable sheets (e.g. Polypropylene or Thermoplastic Polyurethane coated nylon fabric) with a soldering iron mounted on an XY stage (Fig. 2a). By adjusting both the temperature and displacement velocity of the head, one can simply seal or additionally cut along the path. The envelopes obtained are inflated to a typical pressure of 0.1 bar, to ensure the doubly asymptotic regime of interest (inextensibility and vanishing bending stiffness).

We first consider two superimposed flat rings, sealed along both their inner edge R and outer edge $R + w$ (Fig. 2b). We assume that the membrane as well as the seams are inextensible but do not bear any bending rigidity, so that they may freely accommodate excess of material with wrinkles upon inflation. We are here interested in the resulting overall inflated shape (and not in the local morphology of the wrinkles). The deployed surface is assumed to remain axisymmetric. Experiments show that meridians are under tension, whereas radial wrinkles pervade the entire surface of such inflated closed rings (see Fig. 3a), in contrast with open-ended balloons in Fig. 1, which command a different, extended analytical treatment (Section 3).

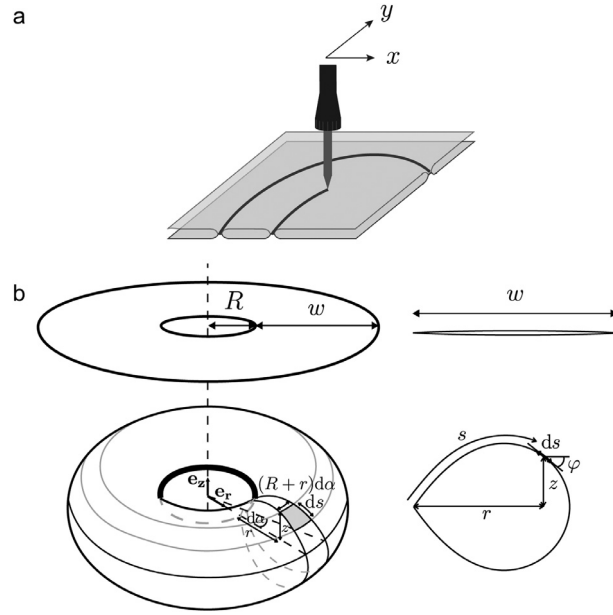


Fig. 2. **a.** Sketch of the fabrication process: a soldering iron is mounted on an XY-plotter, and the desired sealed path is simply printed on two superimposed flat thermoplastic sheets (eg. Polypropylene or Thermoplastic Polyurethane coated nylon fabric). **b.** Sketch of a ring with inner radius R and width w before and after inflation.

2.1. Derivation of the equations using volume maximization

The section of the axisymmetric inflated ring is described by the curvilinear coordinate s along a meridian, the vertical coordinate $z(s)$, the distance to the symmetry axis $R + r(s)$, and the angle φ of the tangent to the meridian line with respect to the auxiliary unit vector \mathbf{e}_r (Fig. 2b). The section is assumed to be symmetrical with respect to the plane $z = 0$. In this framework, the equilibrium shape maximises the volume V of the toroidal shape obtained by rotational symmetry

$$V = 4\pi \int_0^w [R + r(s)]z(s) \cos \varphi \, ds \tag{1}$$

under the inextensibility condition. The inextensibility in the radial direction is simply ensured by the bounds of the integral $s \in [0, w]$ (as we assume that radial lines are not wrinkled). In the azimuthal direction, inextensibility imposes the following inequality

$$\forall s, P(s) \leq P^0(s), \tag{2}$$

where we have defined the apparent perimeter $P(s) = 2\pi (R + r(s))$ of the circle passing through the point of coordinate s of the section, and $P^0(s) = 2\pi (R + s)$ the initial perimeter in the flat state. When $P(s) < P^0(s)$, radial wrinkles absorb the difference between the apparent perimeter $P(s)$ and the actual initial perimeter $P^0(s)$. Here, this continuous inequality can be greatly simplified in the following way: radial inextensibility trivially imposes that $\forall s, dr/ds = \cos \varphi \leq 1$, and thus $dP/ds \leq dP^0/ds$. Therefore Eq. (2) is satisfied if and only if $P(0) \leq P^0(0)$, or equivalently if and only if $r(0) \leq 0$. An optimal solution must equalize the inequality constraint for at least one curvilinear coordinate, and from the previous equation it must be at $s = 0$. The inextensibility condition (2) thus reduces to the simple boundary condition:

$$r(0) = 0 \tag{3}$$

In other words, the inner radius of the ring is preserved when the annulus is inflated.

We have greatly simplified our problem since we now only need to maximize (1) with the boundary condition (3), which is a standard procedure. Nondimensionalizing the lengths by w , the Lagrangian for the optimization problem may be written in terms of dimensionless variables and parameters denoted by $*$:

$$L = 4\pi \int_0^1 [(R^* + r^*)z^* \cos \varphi + A(\cos \varphi - r^{*'}) + B(\sin \varphi - z^{*'})] ds^*, \tag{4}$$

where (\prime) now stands for derivative with respect to s^* . In our derivation, z^* , r^* and φ are seen as independent variables of the minimization problem, whereas A and B are two Lagrange multipliers enforcing the geometrical relations ($r^{*'} = \cos \varphi$

and $z^{*'} = \sin \varphi$. Using classical variational methods, we obtain the following system of equations:

$$\begin{cases} A' = -z^* \cos \varphi \\ B' = -(R^* + r^*) \cos \varphi \\ r^{*'} = \cos \varphi \\ z^{*'} = \sin \varphi \\ [A + z^*(R^* + r^*)] \sin \varphi = B \cos \varphi \end{cases} \quad (5)$$

with the boundary condition $A(1) = 0$ because $r^*(1)$ is free, whereas $r^*(0) = 0$ is fixed by Eq. (3). Symmetry also imposes the boundary condition $z^*(0) = z^*(1) = 0$. We do have the four boundary conditions required to solve the system of four first-order ordinary differential equations:

$$\begin{cases} A(1) = 0 \\ r^*(0) = 0 \\ z^*(0) = 0 \\ z^*(1) = 0 \end{cases} \quad (6)$$

We note that these boundary conditions naturally impose that there is no angle discontinuity at the exterior point $s^* = 1$. Indeed if the boundary conditions $z^*(1) = A(1) = 0$ are inserted in the last equation of (5), we obtain $B \cos \varphi = 0$, which generically leads to $\varphi(1) = \pm \pi/2$: the angle is continuous at this point. This is not the case at the inner point $s^* = 0$, where $A(0)$ has no reason to vanish. Mathematically, this is due to the fact that at the inner seam, the condition $A = 0$ is replaced by the fixed imposed position $r^*(0) = 0$. In physical terms, this fixed position of the inner point $s = 0$ is enforced by an orthoradial line tension, which is necessary to balance forces applied on a kink ($\varphi \neq \pm \pi/2$) in the radial line bearing tension. At the exterior point $s^* = 1$, we have conversely assumed that the membrane does not support any orthoradial tension (it is radially wrinkled) so that no kink is possible. In conclusion, the tear-drop shape of the cross section with a kink at the inner seam (Fig. 3) does not result from different material properties (such as a stiffer seam line) but from the difference in equilibrium conditions in the inner and outer seam.

2.2. Derivation of the equations using force balance.

The same shape of a toroidal balloon, formed by two annular flat rings can be derived with another method based on a force balance on the envelope, in line with the classical parachute shape problem derived by Taylor (1963), Deng (2012). As parachutes should be as light as possible, wrinkles, which mean an excess of material, should be avoided. In order to save most fabric, Taylor computed the flattest possible shape for a parachute, since the drag force is proportional to the projected area of the parachute; the hoop stress should therefore be zero. In addition, the pressure inside the parachute is assumed to be constant. This configuration is therefore equivalent to the shape that would adopt a mylar balloon made of two flat circular disks sealed together along their edges (Paulsen, 1994).

In the deformed state, one can consider an infinitesimal surface dS (Fig. 2b), which is subjected to forces at equilibrium: radial and hoop tensions per unit length in the inflated wrinkled configuration, denoted by T_φ and T_α respectively and the pressure p . We make the analysis in the minimal framework of tension field theory (Mansfield, 1969; 1977) and consider that compressive stresses are prevented in the envelope by wrinkling: the elastic cost of apparent envelope contractions is neglected. As the envelope can also be considered as inextensible in the regime of interest, our analysis is thus purely geometrical. As radial wrinkles are experimentally observed on the whole envelope, we assume that the tension in the hoop direction vanishes: $T_\alpha = 0$.

Equilibrium of a surface element of the envelope in the radial direction leads to

$$\frac{d((R+r)T_\varphi)}{d\varphi} = 0 \quad (7)$$

After integration, we obtain:

$$T_\varphi = \frac{T_0}{R+r} \quad (8)$$

where T_0 is a constant, the tension per unit angle $d\alpha$, that will be determined by the boundary conditions. Following Laplace's law (force balance in the normal direction), with the condition $T_\alpha = 0$, we deduce:

$$p = \kappa T_\varphi \quad (9)$$

where $\kappa = d\varphi/ds$ is the local curvature in the radial direction. Combining, the two last equations in order to eliminate T_φ , we obtain a linear variation of the curvature with the distance r to the axis of symmetry:

$$\frac{d\varphi}{ds} = \frac{p}{T_0} (R+r) \quad (10)$$

which, after being multiplied by $\cos \varphi = dr/ds$, can be integrated into

$$\sin \varphi = -(p/T_0)(R+r)^2/2 + cst \quad (11)$$

It is interesting to show that the equations derived with both methods are equivalent. Differentiating the last equation in the set of Eq. (5) and using the other relations to simplify leads to the equation:

$$\frac{d\varphi}{ds} = -\frac{(R+r)\sin\varphi}{B} \quad (12)$$

Using again Eqs. (5) and (10), it can be shown by differentiation that the quantity $\sin\varphi/B$ is constant. Following Eq. (12), $d\varphi/ds$ is strictly proportional to $(R+r)$, where the constant $\sin\varphi/B$ corresponds in physical terms to $-p/T_0$.

We may also interpret Lagrange parameters A and B that appear in the variational equations by separating an elementary angular sector of the system (membrane + inner fluid) with an imaginary cylindrical cut of radius $R+r_0$ and by considering the force per unit length exerted by the portion $r > r_0$ on the part $r < r_0$.

$$B = T_0/p \sin\varphi, \quad (13)$$

is the vertical projection of the membrane tension per unit angular sector non-dimensionalized by pw . The total dimensionless horizontal force

$$A = T_0/p \cos\varphi - z^* \quad (14)$$

also includes a contribution of the pressure acting on the vertical section, in addition to the projected membrane tension.

2.3. Comparison with experiments

We can solve the boundary value problem (5)–(6) using Matlab function `bvp4c` varying the slenderness ratio S of the ring, $S = R/(R+w) = R^*/(R^*+1)$, and compare the results with cross sections measured experimentally (Fig. 3).

Theoretical predictions (solid lines) are in quantitative agreement with the experimental measurements (triangles). For slender rings (i.e. when $S \rightarrow 1$), the cross section tends to the trivial cross section of a straight inflated path: a circle. In the opposite regime $S \rightarrow 0$, the cross section strongly deviates from a circle and a singularity appears at the inner point $s^* = 0$. This shape may be intuited qualitatively as sketched in Fig. 4. The volume of the toroidal structure is proportional to the product of the area of the cross section with the radius OC of the centroid of this cross section ($OC \in [R, R+w]$). Optimizing the enclosed volume thus corresponds to a compromise between maximizing the area of the cross section, which is obviously obtained with a circular shape, and elongating this circle to increase OC (while maintaining the inner radius R constant). In the limit $w \ll R$, the relative impact of a variation of OC is negligible and therefore the cross section tends to a circle. Conversely, the position of the centroid has a strong impact in the opposite limit $R \ll w$, which leads to an elongated cross section reminiscent of a tear-drop shape (Fig. 4).

In such a configuration of axisymmetric closed rings, inflation induces azimuthal compression everywhere except at the inner radius $s = 0$, since all material points have moved towards the axis of symmetry of the ring ($\forall s \in]0, w], r(s) < s$). The inflated ring presented in Fig. 3a exhibits radial wrinkles accordingly, except in a small region near the inner part of the ring.

Here, the inflated ring has been gently constrained to remain in plane between two PMMA plates. Unconstrained experimental realizations exhibit surprising features. In contrast with the axisymmetric hypothesis, slender rings buckle out of plane (see Fig. 5) and follow a smooth saddle outline with envelopes made of slightly stretchable fabrics or display localized kinks for envelopes made of thin polypropylene. This instability is the imprint of a geometrical frustration of the inflated ring, reminiscent of circular fold origami (Dias et al., 2012; Dias and Santangelo, 2012) or elastic growing rods with incompatible curvature (Moulton et al., 2013). This frustration may be released by cutting the ring radially and sealing the edges (Fig. 6), thus removing the closing condition. As a result, we observe a significant coiling of the structure upon inflation, that we now aim at rationalizing.

3. Inflating open rings

The paradoxical coiling of the structure upon inflation may be qualitatively explained using simple torque balance arguments: in physical terms, having a free end imposes a vanishing total force and internal torque in the section (only the vanishing force condition applies to axisymmetric closed rings). Considering a cut in the $(\mathbf{e}_r, \mathbf{e}_z)$ plane, the pressure force acting on one half of the ring is pA where A is the area of the two cross sections. In closed configurations, the membrane tension balancing this separating pressure force is entirely supported by the inner seam, as all other points of the membrane are under hoop compression and bear no azimuthal load. However, the pressure moment with respect to the inner seam is not balanced. This moment induces the coiling of the structure until two up-down symmetric lines (or bands) of tension appear and provide internal torque balance.

3.1. Volume maximization of an open ring

The coiling angle has been estimated in reference (Siéfert et al., 2019b) using the crude approximation that azimuthal tension was always reduced to a pair of (up-down symmetric) lines. However, this approximation fails for non-slender rings. Here, we wish to describe quantitatively this phenomenon, using the correct inextensibility condition in the optimization

of the volume. We define the strain $\lambda = \alpha/\alpha_0$, where α_0 and α are respectively the angles between two radii at rest and when inflated (Fig. 6). We propose to solve the optimization problem for a given strain and search for which specific value of λ_{\max} the volume is maximized. Assuming that the inner radius remains under azimuthal tension, length conservation imposes a new inner radius $R_1 = R/\lambda$. Because of the coiling of the structure, the azimuthal condition of inextensibility cannot be reduced to an equality condition at one point, as in the closed ring configuration. The apparent perimeter now reads $P(s) = 2\pi\lambda(R/\lambda + r)$ and may exceed the rest perimeter $P^0(s) = 2\pi(R + s)$ for large enough values of λ . We should thus enforce the incompatibility inequality at every point of the envelope. We define the dimensionless azimuthal extension $u^* = (P(s) - P^0(s))/(2\pi w) = \lambda r^* - s^*$, which is negative when the membrane is locally wrinkled (i.e. under compression) and vanishes when the membrane is under azimuthal tension. From the assumption of azimuthal tension at the inner radius, we have $u^*(0) = 0$. Strictly positive values of u^* are forbidden by inextensibility. We account for this condition by a penalty method and add in the Lagrangian function a soft regularization term $-\exp^{\beta u^*}$ where β is a large numerical number. We have verified that the results do not depend on the value chosen for β .

While any azimuthal extension (i.e. any $u^* > 0$) is strongly penalized, this new term almost vanishes and does not play any significant role for compressive states ($u^* < 0$). Replacing the dimensionless radial coordinate r^* by the azimuthal extension u^* and adding the coiling strain λ in our computations, the Lagrangian now reads:

$$L = 4\pi\lambda \int_0^1 \left[\frac{R^* + s^* + u^*}{\lambda} z^* \cos \varphi + A \left(\cos \varphi - \frac{1 + u^{*'}}{\lambda} \right) + B(\sin \varphi - z^{*'}) - \exp^{\beta u^*} \right] ds^* \quad (15)$$

where ($'$) stands for derivative with respect to s^* . Using classical variational methods, we obtain the following system of equations:

$$\begin{cases} A' = -z^* \cos \varphi \\ B' = -u^* \cos \varphi - 1 \\ r^{*'} = \cos \varphi + \beta \exp^{\beta u^*} \\ z^{*'} = \sin \varphi \\ \left[A + z^* \frac{R^* + s^* + u^*}{\lambda} \right] \sin \varphi = B \cos \varphi \end{cases} \quad (16)$$

together with the boundary conditions:

$$\begin{cases} A(1) = 0 \\ u^*(0) = 0 \\ z^*(0) = 0 \\ z^*(1) = 0 \end{cases} \quad (17)$$

This set of equations is solved for varying values of λ , and we verified that for high enough values of the coefficient β (typically $\beta > 1000$), the computed solutions barely depend on its value. A family of profiles corresponding to $S = 0.1$ is presented in Fig. 7a. The profile does not significantly evolve with increasing coiling factor λ until compression at a point $\tilde{s}^* > 0$ vanishes (i.e. $u^*(\tilde{s}^*) = 0$ as shown in Fig. 7b). A flat tilted region under biaxial tension appears and grows with λ . Tension in both directions ensures that the flat metric is preserved in this region. This tilted portion forms an angle $\gamma = \arccos \lambda^{-1}$ with the horizontal axis; the same cone angle emerges when a flat circular ring (or disc) of paper is radially cut and over-curved into a conical annulus (or cone), since the conical geometry is prescribed in both cases by inextensibility (or isometry). Each solution tends to maximize the volume given an imposed coiling factor λ . The cross-section profile evolves significantly in this regime, the outer seam getting closer to the inner seam. Plotting the evolution of the volume as a function of the coiling factor (Fig. 7c), a maximum appears for a coiling factor λ_{\max} which depends on the slenderness S of the open ring.

We verify experimentally, using the same methods as for closed rings, that the structures naturally select this optimal solution, exhibiting the predicted cross-section profile and – coiling by a factor λ_{\max} . The difference between closed and open ring cross sections is shown in Fig. 8 for $S = 0.1$. In this case of thick open annuli (S close to 0), the inner radius R is small compared to the width w . Experiments with such open structures require special caution. End effects are important if the extremities of the envelope are simply sealed. To ensure that the ends of the open ring do not influence the experimental measurements, flat rigid panels with a shape close to the theoretically predicted cross section are sealed at both ends of the open ring, as shown in Fig. 8b. The superimposition of theory (dashed lines) and experiments (light red line) shows a remarkable quantitative agreement for both open and closed rings (Fig. 8c and d) for $S = 0.1$. We obtain the same agreement with configurations involving different values of S that are plotted in Fig. 9. The model reproduces accurately the experimental cross sections, and even renders the small discrepancies observed between open rings of varying slenderness S . The cross sections in the open configuration appear to be less pointed, and overall much closer to the circle for any slenderness (Fig. 9) than for the case of closed rings (Fig. 3), even if they include flat portions with azimuthal tension.

3.2. Coiling factor

We present in Fig. 10 the evolution of the coiling factor λ as a function of the slenderness ratio S . Two series of specimens were made of $4 \mu\text{m}$ thick polyethylene and $16 \mu\text{m}$ thick polypropylene, respectively. In contrast with Siéfert et al. (2019b),

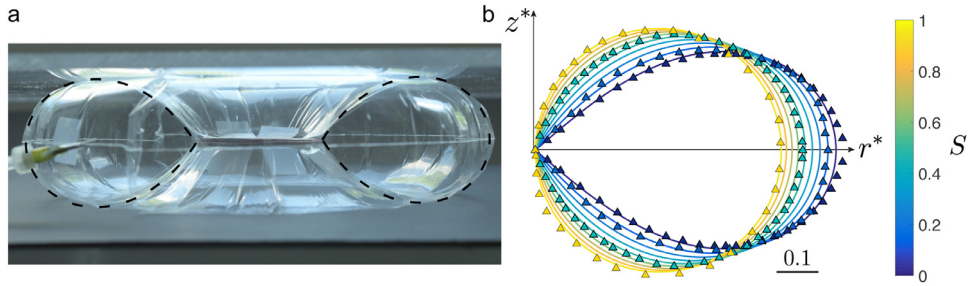


Fig. 3. Cross-section of a closed inflated annulus. **a.** Profile picture of a closed inflated annulus. The axisymmetry of the structure is constrained by two plates to prevent out-of-plane buckling. Radial wrinkles extend here along all the membrane. The ring is made of a $16\mu\text{m}$ thick polypropylene sheet of inner radius $R = 25\text{ mm}$ and outer radius $R + w = 130\text{ mm}$. Dashed lines correspond to the theoretical cross sections. Note that the wrinkles extend through the whole torus. **b.** Theoretical (solid lines) and experimental (triangles) rescaled cross sections of inflated closed rings for various aspect ratios $S = R^*/(1 + R^*)$ with $R^* = R/w$. $r^* = r/w$ and $z^* = z/w$ correspond to the rescaled radial and vertical coordinates, respectively.

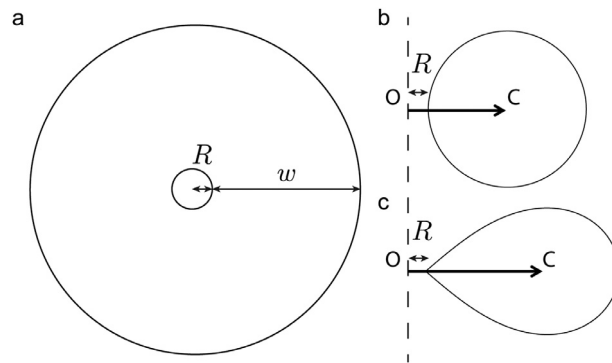


Fig. 4. For a non slender ring ($S \rightarrow 0$) (a), the maximization of the volume may be seen as a compromise between having an optimal circular cross section area (b) and having the largest possible mean radius OC (c), as the global volume scales as the product of both quantities.

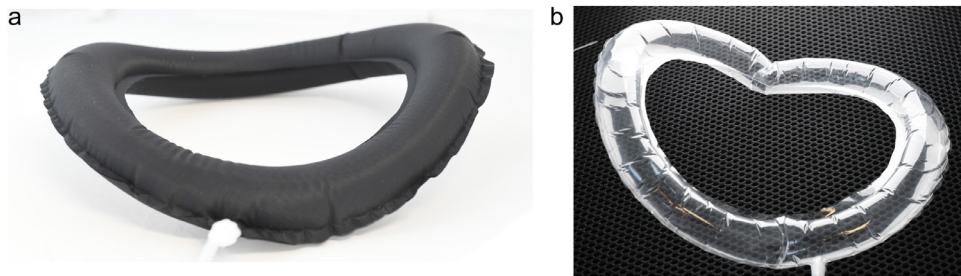


Fig. 5. Upon inflation, an unconstrained ring buckles out of plane. In the case of a ring made from a fabric that allows slight shear compliance (Boisse et al., 2011), the structure is smooth (a). Conversely, two opposite folds appears in rings obtained with thin polypropylene sheets (b).

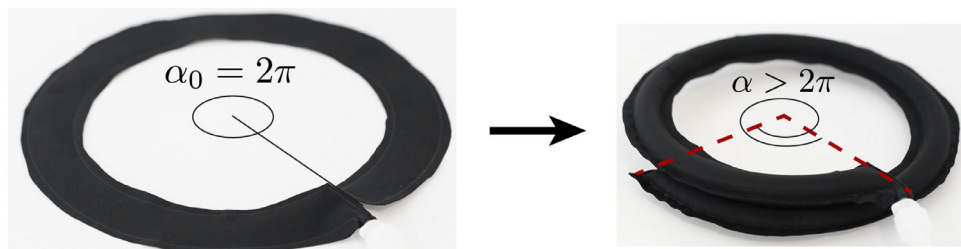


Fig. 6. When an open ring is inflated, the structure over-curves and exhibits overlapping.

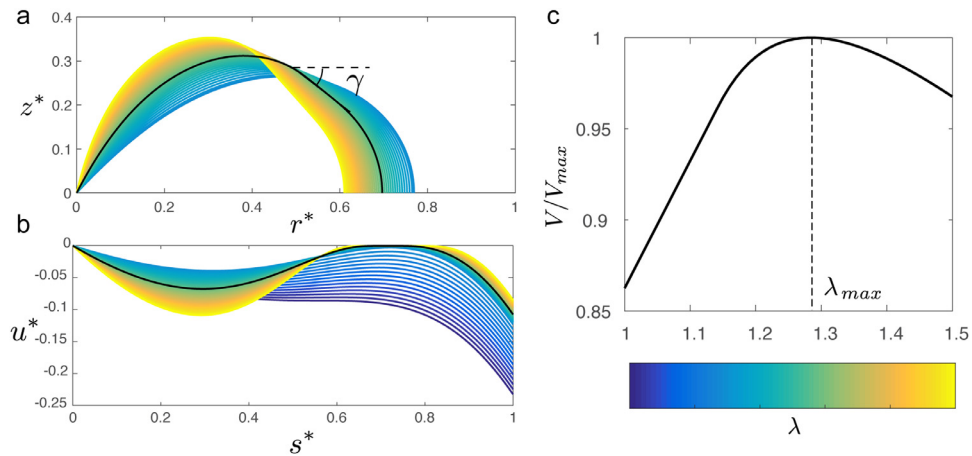


Fig. 7. Theoretical dependence of the geometry of the inflated ring as a function of over-curvature. **a.** Rescaled theoretical profiles for over-curvature factors λ varying from 1 to 1.5 for a slenderness ratio $S = 0.1$. The black line corresponds to the profile for $\lambda_{\max} = 1.28$ that maximises the total volume. **b.** Rescaled perimeter contraction u^* as a function of the curvilinear coordinate s^* . When over-curvature is increased, a non-compressed portion of the membrane appears and then expands. As a general trend, the profile is almost the same as in the axisymmetric configuration in the absence of tension lines (minors differences result from the fact that the inner radius is not R anymore but R/λ). When compression vanishes at one point (highlighted by the black dashed line) for $\lambda \approx 1.16$, the condition $u^* \leq 0$ becomes dominant and induces the formation of a band under tension (the straight portion of the profile around $r^* \sim 0.6$). The angle of the tangent to this band with the horizontal is geometrically set to $\gamma = \arccos(1/\lambda)$. The portion under tension extends until an optimal volume is encompassed. **c.** Evolution of the volume as a function of the over-curvature factor λ . Volume is maximised for an over-curvature factor λ_{\max} that depends on the slenderness S of the structure. For $S = 0.1$, $\lambda_{\max} \approx 1.28$.

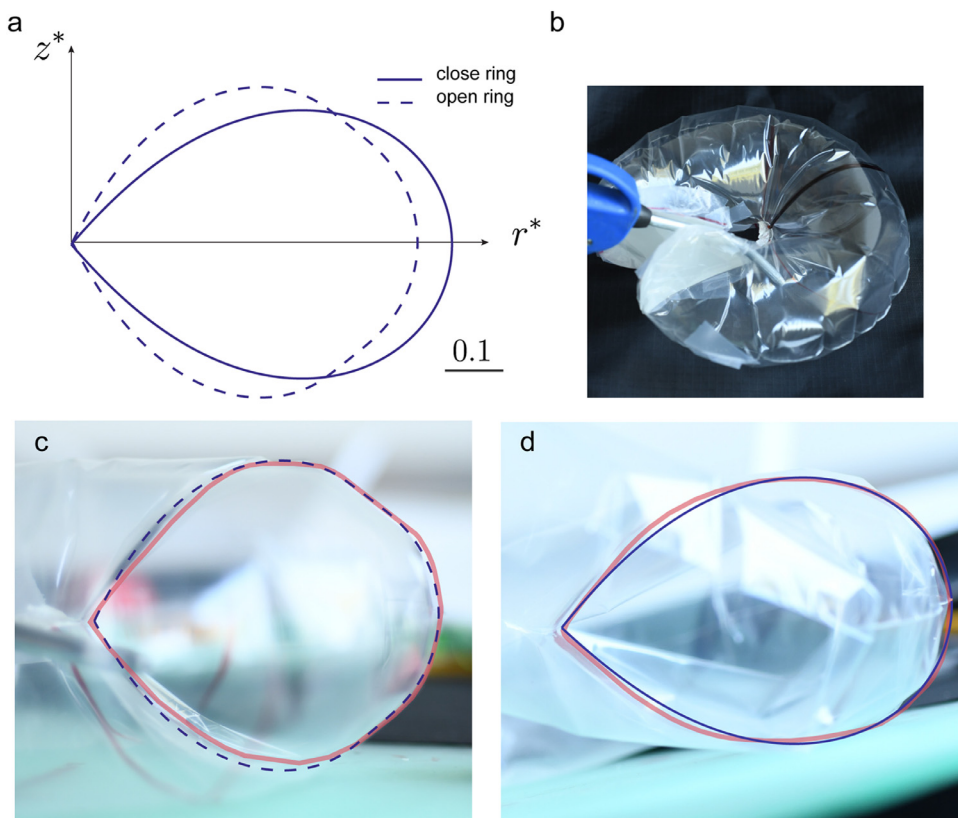


Fig. 8. Comparison of the cross section of the ring in open or closed configurations for a slenderness $R^*/(R^* + 1) = 0.1$ (we find that $\lambda_{\max} = 1.28$). **a.** Theoretical predictions: the shapes are significantly different in closed (solid line) and open (dashed line) conditions. **b.** Picture of an inflated open ring. In order to avoid boundary effects, flat rigid panels of the shape of the predicted cross section are sealed on both ends of the open ring. **c-d.** Overlay of the experiments (red line on the picture) and the theoretical curves (blue lines) for (c) open and (d) closed conditions. (For interpretation of the references to colour in this figure legend, the reader is referred to the web version of this article.)

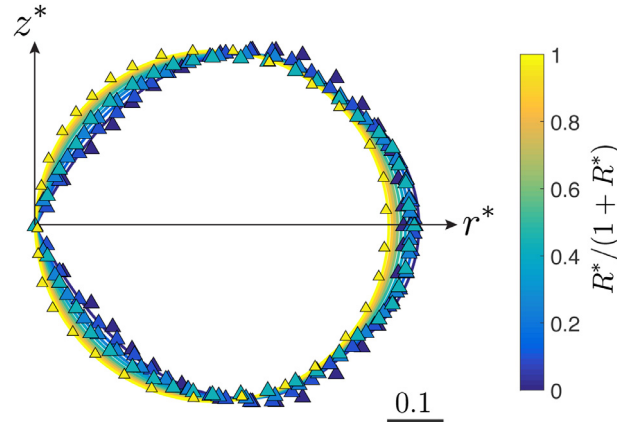


Fig. 9. Experimental and theoretical profiles. The theoretical results from the Lagrangian derivation describe accurately the experimental cross sections. Contrary to the closed ring configuration presented in Fig. 3, the overall global shape of profiles for open rings does not significantly depend on the slenderness ($R^*/(R^* + 1)$) although the width of the flat bands that are now present may vary.

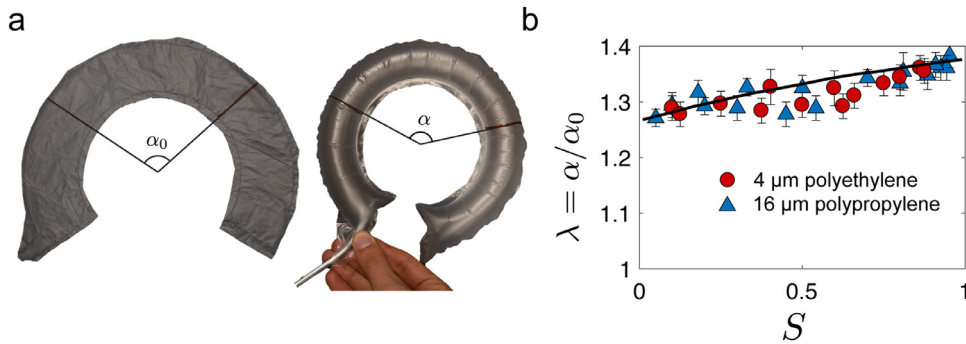


Fig. 10. **a.** Picture of a flat curved path, before and after inflation: the inflated structure coils, inducing an over-curvature $\lambda = \alpha/\alpha_0$. **b.** Coiling factor λ as a function of the slenderness ratio S : triangles and circles represent actual experiments with curved paths made of $4\ \mu\text{m}$ thick polyethylene and $16\ \mu\text{m}$ thick polypropylene sheets respectively. The black line is the theoretical prediction based on our model.

where the prediction failed for non slender rings ($R^* < 2$), we obtain here a quantitative agreement between experiments and theory for a whole range of slenderness, the strain λ monotonically varying from 1.28 to 1.38.

In the limit of high slenderness ($S^* \rightarrow 1$), the profile of the section is circular, and we can obtain direct estimates for all these quantities. The dimensionless contraction may in this case be analytically derived and reads $u_\lambda^*(s) = \lambda[1 - \cos(\pi s^*)] - s^*$. In this case, the width of the unwrinkled band vanishes. The optimal λ is thus obtained when a single tension line appears at a curvilinear coordinate \bar{s}^* . Such coordinate obey the following equations:

$$u^*(\bar{s}^*) = 0 ; u^{*'}(\bar{s}^*) = 0 \tag{18}$$

For a circular section, the position of the tension line satisfies the transcendental equation $\pi s^* \sin(\pi s^*) = 1 - \cos(\pi s^*)$ that we solve numerically. We obtain the position of the tension line at $s^* = 0.74$ with a relative curvature increase $\lambda = 1.38$ in agreement with our numerical estimates.

3.3. Morphology of mylar balloons

We now report consequences of these calculations on the morphology of mylar balloons: the shape of the inflated envelope and the distribution of wrinkles. The over-curvature predicted above explains why commercially available mylar balloon letters are cut along peculiar shapes; they are empirically designed to compensate for over-curving. For instance, the “9” balloon in Fig. 1 does not include any self-contact before inflation. The letter “O” has, before inflation, a missing angular sector, and rather looks like a “C” (Pak, 2006) (see Fig. 11a). If the balloon were made out of flat closed annuli, it would buckle out of plane, as shown earlier.

We note that radial wrinkles appear on the surface except along the inner radius and on symmetric bands (Fig. 11b). In our computations, the function u^* is a measure of the local azimuthal compression and should indicate the presence (or absence) of wrinkles (Aharoni et al., 2017; Cerda and Mahadevan, 2003). The experimental extent of the unwrinkled band should correspond to the region where the function u^* is found to be close to zero. We show in Fig. 11b a remarkable agreement between both features. The width of this band decreases with increasing slenderness, as shown in Fig. 11c.

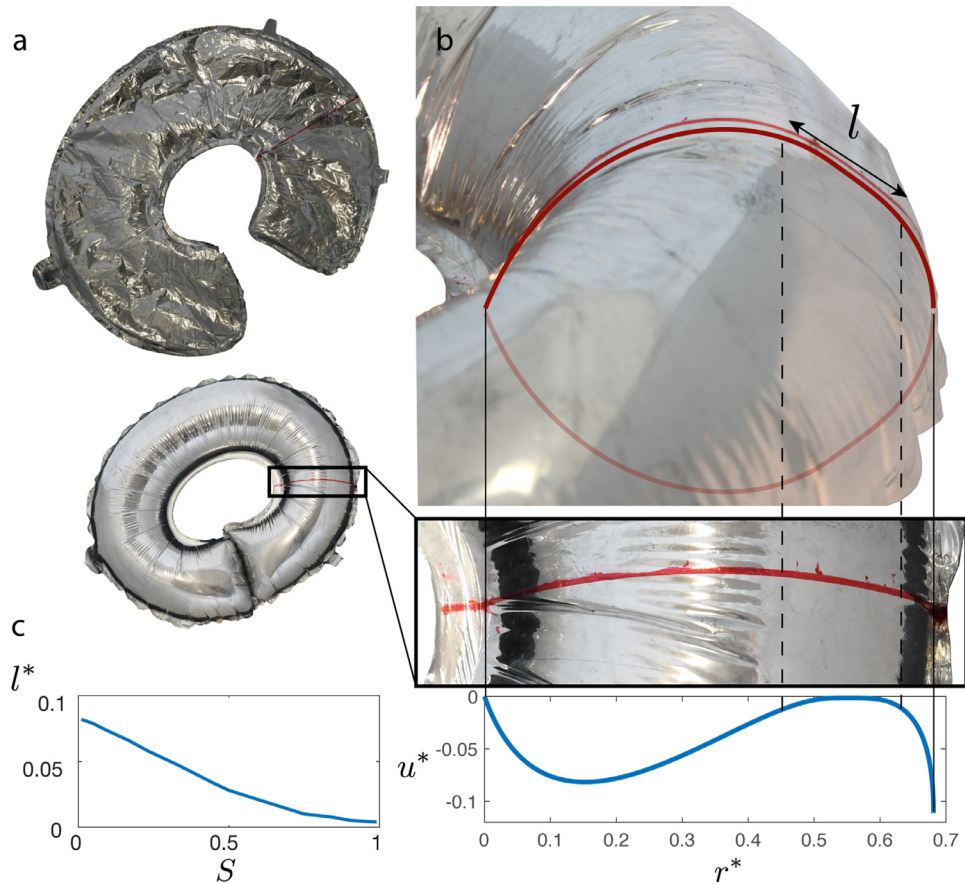


Fig. 11. Wrinkle pattern on a commercial “O” mylar balloon. **a.** Upon inflation, a flat “C” path coils and form the letter “O”. **b.** Superposition of the predicted profile on a picture of the balloon, at a point where the local slenderness $R^*/(R^* + 1) = 0.26$. The envelope presents wrinkles on most of its surface. However, circular smooth bands are observed. The location of these bands can be interpreted as the region where the compression of the perimeter u^* is close to vanish. **c.** Theoretical dimensionless extension of the unwrinkled band $l^* = l/w$ as a function of the slenderness.

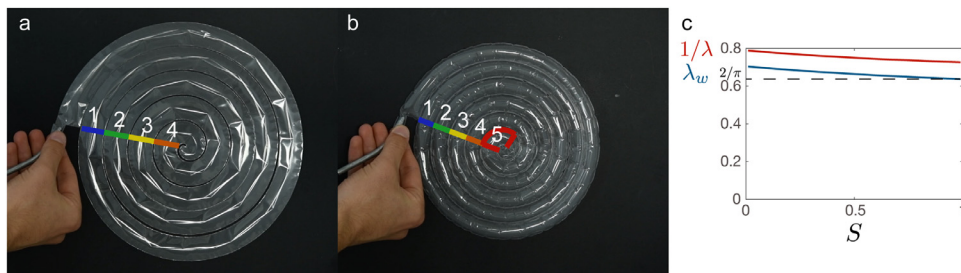


Fig. 12. Coiling of an archimedean spiral. **a.** Initial flat structure. The spiraling path is cut along the seam line. **b.** Structure after inflation, exhibiting a strong coiling of approx. 480° (See Supplementary Video 1). **c.** Theoretical inner radius of curvature change $1/\lambda$ and in-plane radial contraction $\lambda_w = r_{\max}^* = r^* (s^* = 1)$ as a function of the slenderness.

However, many features of these inflated curvilinear balloons remain misunderstood: the alternation of smooth wrinkles and crumples is not captured by our model (see Fig. 11b). We did not investigate neither the selected wavelength of the wrinkles nor the impact of curvature on those. Numerous recent studies have been tackling these challenges in slightly different configurations (King et al., 2012; Paulsen, 2019; Paulsen et al., 2017; Timounay et al., 2020).

4. Inverse problem for programming any arbitrary 2D path

Having rationalized the change in curvature for open circular rings of constant curvature, we can extend our analysis to any planar path of varying curvature. Our aim is to solve the inverse problem, i.e. determining the initially flat template that

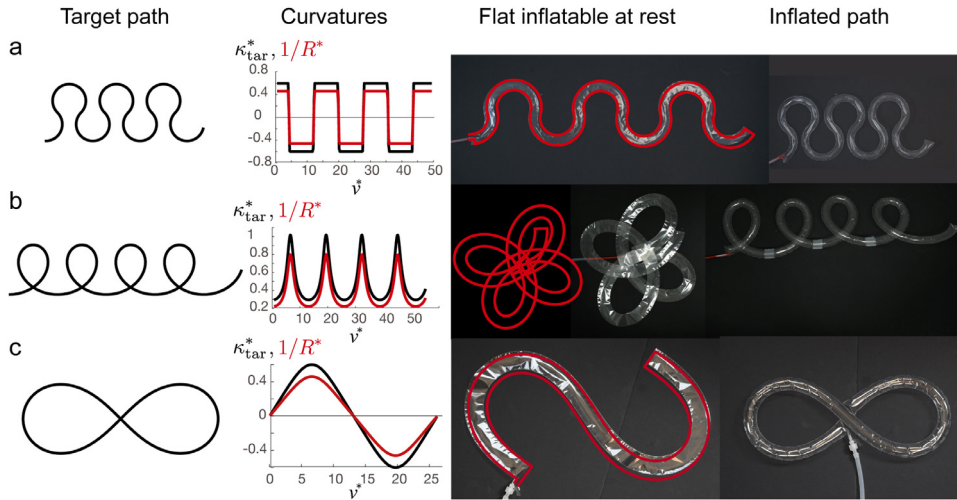


Fig. 13. Inverse problem: simple analytic examples. **a.** Alternate constant curvature: the structure contracts upon inflation. **b.** Loops: varying positive curvature. The compact structure expands into a cycloidal pattern. **c.** Lemniscate obtained from a “S” shape. From left to right: target path; normalized target and rest curvature κ_{tar}^* and $1/R^*$ for a given path width w , as a function of the curvilinear coordinate $v^* = v/w$ (the curvature of the flat path is computed using the prediction for curvature change plotted in Fig. 10b); flat path computed with the inverse model superimposed on a picture of the experimental realization; same path under pressure, matching closely the target curve.

will lead to any arbitrary 2D structure upon inflation. The case of a slenderness ratio close to unity has been presented in a previous study (Siéfert et al., 2019b). We propose here to extend this approach to any value of S .

An interesting example to start with is a disk cut and sealed along an archimedean spiral, corresponding to a linearly increasing radius of curvature. We observe that the whole structure coils by more than a complete loop (Fig. 12 and Supplementary Video 1) as expected from theory. Moreover, the inflated structure almost fills the plane, without overlap nor gaps between two successive turns. Upon inflation, the in-plane radial distance between inner and outer seam lines of a path indeed reduces from 1 to $\lambda_w = r^*(s^* = 1)$ in dimensionless coordinates (Fig. 12c). At a specific dimensionless radius R^* of the archimedean spiral, the inner seam contracts radially, as seen before, by a factor $\lambda^{-1}(R^*)$. In the flat configuration, this inner seam coincides with the outer seam of the previous turn of the spiral (at the radius $R^* - 1$). After inflation, its dimensionless radial coordinate reads $(R^* - 1)/\lambda(R^* - 1) + \lambda_w(R^* - 1)$ which is very close to $\lambda^{-1}(R^*)R^*$ since (i) λ^{-1} is close to λ_w and (ii) λ^{-1} does not vary significantly with S . In fact, if the outer boundary were under tension $u^*(s^* = 1) = \lambda r^* - s^* = 0$, the boundary condition would exactly read $r^*(1) = \lambda^{-1} = \lambda_w$. We conclude that the equality does not hold but is close because u^* remains small (see Fig. 11(b)). The case where the radial contraction equals the width reduction has the geometrical property that the annulus seems to undergo a global shrinking factor λ^{-1} (but because the curvilinear length is conserved there is an overpassing).

We propose now to use our geometrical model to solve the inverse problem. We start with a simple path with dimensionless curvature constant by part $\pm \kappa_{tar}$ (portions of circles: Fig. 13a and Supplementary Video 2). We define the parameter v^* as the curvilinear coordinate v along the path to be programmed normalized by the width w . Using the results plotted in Fig. 10b, we simply find the normalized curvature $1/R^*$ that, when coiling by a factor λ_{R^*} , reaches the target curvature κ_{tar} . In other words, we numerically solve the relationship:

$$\frac{\lambda(R^*)}{R^*} = \kappa_{tar}^*. \quad (19)$$

where the function $\lambda(R^*)$ is plotted in Fig. 10b as a function of $S = R^*/(R^* + 1)$ instead of R^* . The dimensionless target curvature κ_{tar}^* and rest curvature $1/R^*$ are plotted in Fig. 13, second column, as a function of the curvilinear coordinate v^* . The curvature in the flat state $1/R^*$ is typically smaller than the target curvature κ_{tar}^* , by a factor λ varying between 1.28 and 1.38 depending on the target curvature. We then plot the curvature profile $1/R^*(v^*)$, starting at an arbitrary position and orientation. In order to account for the width of the path, we shift the computed curve by $\pm w/2$ in the normal direction. The same parametrization may be used in the flat state as in the target inflated state because (i) the inner edge, under tension, preserves its length and (ii) the path is chosen relatively slender ($\kappa_{tar}^* \ll 1$).

Extending the inverse problem to paths with continuously varying curvatures, such as a sequence of loops (Fig. 13b and Supplementary Video 3), we first compute the curvature $\kappa_{tar}(v^*)$ of the target path. The normalized radius of curvature $R^*(v^*)$ of the corresponding flat ribbon is obtained by numerically solving Eq. (19) for each curvilinear coordinate v^* (Fig. 13b, second column). The outline of the deflated balloon is plotted with the correct curvature $\kappa(v^*) = 1/(wR^*(v^*))$ and offset with $\pm w/2$ (Fig. 13b, third column). As overlap occurs in the flat configuration, the path is printed using several non overlapping distinct parts, that are bonded together using tape. Upon inflation, the flat four-leaf clover-like structure coils into the sought sequence of loops with good precision (Fig. 13b, fourth column). A lemniscate is programmed with the same

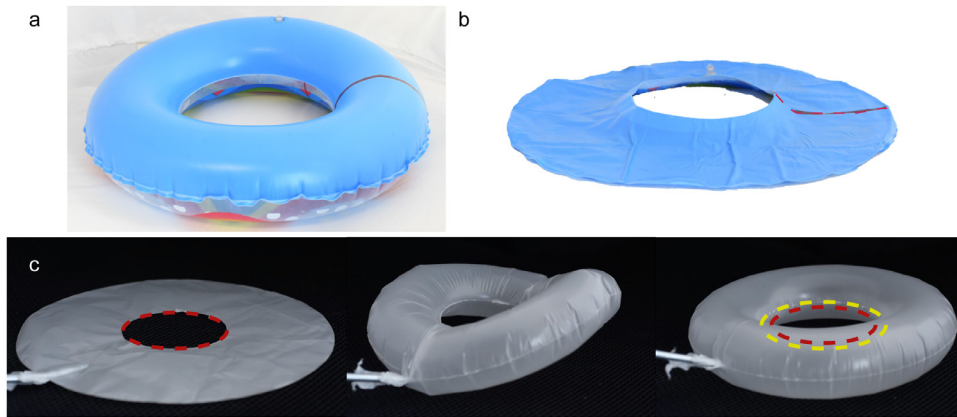


Fig. 14. Swim rings. **a.** Inflated commercial swim ring with radial wrinkles concentrated at the outer edge. **b.** The deflated envelope of the swim ring is not flat. **c.** From left to right: flat annulus before inflation; buckled structure for intermediate pressures; planar swim ring for high pressure. Note the significant stretching of the inner seam (the red dashed lines corresponding to the initial and the yellow one to the inflated inner perimeter). Wrinkles are not present in the inner part of the swim ring, indicating tension in the sheet. (For interpretation of the references to colour in this figure legend, the reader is referred to the web version of this article.)

procedure in Fig. 13c. Depending on the choice of the target path, inflation of the structure may induce rotation (Fig. 12), contraction (Fig. 13a), expansion (Fig. 13b) and self closing (Fig. 13c).

Our theory is rigorously valid only in the case of slowly varying curvatures ($d\kappa_{\text{tar}}/dv^* \ll 1$), i.e. when the outline of the path may be locally seen as a path of constant curvature. As cross sections do not significantly depend on the slenderness ratio S (and equivalently on the rescaled radius of curvature R^* , as shown in Fig. 9), we may assume that the coiling factor λ computed for constant curvature open rings still holds locally and that the inverse programming is not too sensitive to sharp variations in the target curvature κ_{tar} .

5. Discussion and conclusion

In this article, we have studied the geometrically non-linear problem of finding the equilibrium shape of an inflated pair of flat slender ribbons sealed along their edges. We extended, deepened and gave a complete resolution (instead of approximations) to the experimental results from Siéfert et al. (2019b). Using two different methods, we derived the cross-section shape of inflated closed rings. Their surprising buckling is explained by their incompatible curvature, readily assessed when the ring is cut. The theory for open rings, using a regularization term, predicts accurately the cross-section profiles, the coiling factor λ and the size of the unwrinkled band for any slenderness. This allows us to solve the inverse problem, i.e. to program with quantitative agreement the target shapes of any path.

The stiffness of such inflated beam-like structures is not tackled in this study, since we focused on a doubly asymptotic regime, where bending energy vanishes and stretching energy diverges. More precisely, the presence of radial wrinkles over most of the structure, should certainly impact the homogenized bending stiffness of such structures.

Finally, the following question naturally arises: why do commercial swim rings remain in plane and do not buckle when inflated (Fig. 14a)? This question may be addressed by deflating a commercial swim ring (Fig. 14b): the deflated annulus is not flat, but exhibits a large radial slope near the inner radius. The metric of the deflated swim ring thus almost coincides with the inflated configuration, except at the outer edge: this is the reason why wrinkles appear solely at the outer edge (see Fig. 14a). It is however highly unlikely, that these rest shapes are precisely manufactured. Inflating flat samples with high enough pressures does lead to the same result. At intermediate pressure, when the inextensibility assumption still holds, the ring buckles out of plane. At higher pressure however, the inner seam, under diverging hoop stress in our quasi-inextensible model, significantly stretches (highlighted in Fig. 14c) and the structure becomes axisymmetric again. The prediction of the typical pressure for which the structure returns in-plane is challenging and could be adapted from recent studies on hyperelastic toroidal structures (Roychowdhury and DasGupta, 2015; 2018). Using a plastic material (in our case polyethylene), it is then possible to fabricate axisymmetric swim rings that present almost no wrinkles, by applying a large pressure load that plastically deforms the initially flat rings (see Fig. 14c).

Declaration of Competing Interest

We declare NO competing interests.

CRediT authorship contribution statement

Emmanuel Siéfert: Conceptualization, Methodology, Investigation, Formal analysis, Writing - original draft. **José Bico:** Conceptualization, Methodology, Investigation, Formal analysis, Writing - original draft. **Etienne Reyssat:** Formal analysis, Writing - review & editing. **Benoît Roman:** Conceptualization, Formal analysis, Writing - original draft.

Acknowledgment

This work was partially funded by the [French Agence Nationale de Recherche](#) (ANR), project SMaRT (ANR-15-CE08-0007). The authors thank Corrado Maurini for enlightening discussions and the anonymous reviewers for their relevant comments.

Supplementary material

Supplementary material associated with this article can be found, in the online version, at doi:[10.1016/j.jmps.2020.104068](https://doi.org/10.1016/j.jmps.2020.104068).

References

- Aharoni, H., Todorova, D.V., Albarrán, O., Goehring, L., Kamien, R.D., Katifori, E., 2017. The smectic order of wrinkles. *Nat. Commun.* 8, 15809.
- Boisse, P., Hamila, N., Vidal-Sallé, E., Dumont, F., 2011. Simulation of wrinkling during textile composite reinforcement forming. influence of tensile, in-plane shear and bending stiffnesses. *Compos. Sci. Technol.* 71 (5), 683–692.
- Cerda, E., Mahadevan, L., 2003. Geometry and physics of wrinkling. *Phys. Rev. Lett.* 90 (7), 74302.
- Chater, E., Hutchinson, J., 1984. On the propagation of bulges and buckles. *J. Appl. Mech.* 51 (2), 269–277.
- Deng, X., 2012. Clefted Equilibrium Shapes of Superpressure Balloon Structures. California Institute of Technology.
- Dias, M., Dudte, L., Mahadevan, L., Santangelo, C., 2012. Geometric mechanics of curved crease origami. *Phys. Rev. Lett.* 109 (11), 114301.
- Dias, M.A., Santangelo, C.D., 2012. The shape and mechanics of curved-fold origami structures. *EPL (Europhys. Lett.)* 100 (5), 54005.
- Hawkes, E.W., Blumenschein, L.H., Greer, J.D., Okamura, A.M., 2017. A soft robot that navigates its environment through growth. *Sci. Rob.* 2 (8).
- Kiefner, J., 1973. Failure stress levels of flaws in pressurized cylinders. In: *Progress in Flaw Growth and Fracture Toughness Testing*, pp. 461–481.
- King, H., Schroll, R.D., Davidovitch, B., Menon, N., 2012. Elastic sheet on a liquid drop reveals wrinkling and crumpling as distinct symmetry-breaking instabilities. *Proc. Natl. Acad. Sci.* 109 (25), 9716–9720.
- Kyriakides, S., Yu-Chung, C., 1991. The initiation and propagation of a localized instability in an inflated elastic tube. *Int. J. Solids Struct.* 27 (9), 1085–1111.
- Ligaro, S., Barsotti, R., 2008. Equilibrium shapes of inflated inextensible membranes. *Int. J. Solids Struct.* 45 (21), 5584–5598.
- Mansfield, E.H., 1969. Tension field theory, a new approach which shows its duality with inextensional theory. In: Hetényi, M., Vincenti, W.G. (Eds.), *Applied Mechanics*. Springer Berlin Heidelberg, Berlin, Heidelberg, pp. 305–320.
- Mansfield, E.H., 1977. Analysis of wrinkled membranes with anisotropic and nonlinear elastic properties. *Proc. R. Soc. London A* 353 (1675), 475–498.
- Moulton, D., Lessinnes, T., Goriely, A., 2013. Morphoelastic rods. Part i: a single growing elastic rod. *J. Mech. Phys. Solids* 61 (2), 398–427.
- Pagitz, M., Pellegrino, S., 2007. Buckling pressure of ‘pumpkin’ balloons. *Int. J. Solids Struct.* 44 (21), 6963–6986.
- Pagitz, M., Pellegrino, S., 2007. Shape optimization of “pumpkin” balloons. In: *AIAA Balloon Systems Conference*, p. 2606.
- Pak, I., 2006. Inflating Polyhedral Surfaces. Preprint, Department of Mathematics, MIT.
- Paulsen, J.D., 2019. Wrapping liquids, solids, and gases in thin sheets. *Annu. Rev. Condens. Matter Phys.* 10, 431–450.
- Paulsen, J.D., Démary, V., Toga, K.B., Qiu, Z., Russell, T.P., Davidovitch, B., Menon, N., 2017. Geometry-driven folding of a floating annular sheet. *Phys. Rev. Lett.* 118 (4), 48004.
- Paulsen, W., 1994. What is the shape of a mylar balloon? *Am. Math. Month.* 101 (10), 953–958.
- Pellegrino, S., 2014. *Deployable Structures*, vol. 412. Springer.
- Roychowdhury, S., DasGupta, A., 2015. Inflating a flat toroidal membrane. *Int. J. Solids Struct.* 67, 182–191.
- Roychowdhury, S., DasGupta, A., 2018. Symmetry breaking during inflation of a toroidal membrane. *J. Mech. Phys. Solids* 121, 328–340.
- Rus, D., Tolley, M.T., 2015. Design, fabrication and control of soft robots. *Nature* 521 (7553), 467.
- Serruys, P.W., De Jaegere, P., Kiemeneij, F., Macaya, C., Rutsch, W., Heyndrickx, G., Emanuelsson, H., Marco, J., Legrand, V., Materne, P., et al., 1994. A comparison of balloon-expandable-stent implantation with balloon angioplasty in patients with coronary artery disease. *N. Engl. J. Med.* 331 (8), 489–495.
- Shepherd, R.F., Ilievski, F., Choi, W., Morin, S.A., Stokes, A.A., Mazzeo, A.D., Chen, X., Wang, M., Whitesides, G.M., 2011. Multigait soft robot. *Proc. Natl. Acad. Sci.* 108 (51), 20400–20403. doi:[10.1073/pnas.1116564108](https://doi.org/10.1073/pnas.1116564108).
- Siéfert, E., Reyssat, E., Bico, J., Roman, B., 2019. Bio-inspired pneumatic shape-morphing elastomers. *Nat. Mater.* 18 (1), 24.
- Siéfert, E., Reyssat, E., Bico, J., Roman, B., 2019. Programming curvilinear paths of flat inflatables. *Proc. Natl. Acad. Sci.* 116 (34), 16692–16696.
- Skouras, M., Thomaszewski, B., Kaufmann, P., Garg, A., Bickel, B., Grinspun, E., Gross, M., 2014. Designing inflatable structures. *ACM Trans. Graph.* 33 (4), 63:1–63:10. doi:[10.1145/2601097.2601166](https://doi.org/10.1145/2601097.2601166).
- Steigmann, D., 1990. Tension-field theory. *Proc. R. Soc. London A* 429 (1876), 141–173.
- Tamadapu, G., DasGupta, A., 2013. Finite inflation analysis of a hyperelastic toroidal membrane of initially circular cross-section. *Int. J. Non Linear Mech.* 49, 31–39.
- Taylor, G., 1963. On the shapes of parachutes. In: *The scientific papers of Sir G.I. Taylor*, vol. 3, pp. 26–37.
- Timounay, Y., De, R., Stelzel, J.L., Schrecengost, Z.S., Ripp, M.M., Paulsen, J.D., 2020. Crumples as a generic stress-focusing instability in confined sheets. *Phys. Rev. X* 10 (2), 21008.